Epitaxial aluminum layer on antimonide heterostructures for exploring Josephson junction effects

W. Pan[1], K.R. Sapkota[2], P. Lu[2], A.J. Muhowski[2], W.M. Martinez[2], C.L.H. Sovinec[2], R. Reyna[2], J.P. Mendez[2], D. Mamaluy[2], S.D. Hawkins[2], J.F. Klem[2], L.S.L. Smith[1,3], D.A. Temple[3], Z. Enderson[4,5], Z. Jiang[5], and E. Rossi[6]

[1]Sandia National Labs, Livermore, California 94550, USA
[2]Sandia National Labs, Albuquerque, New Mexico 87123, USA
[3]Department of Physics, Norfolk State University, Norfolk, Virginia 23504, USA
[4]Oak Ridge Institute for Science and Education Postdoctoral Fellowship, Oak Ridge, Tennessee 37831, USA
[5]School of Physics, Georgia Institute of Technology, Atlanta, Georgia 30332, USA
[6]Department of Physics, William & Mary, Williamsburg, Virginia 23187, USA

Abstract

In this article, we present results of our recent work of epitaxially-grown aluminum (epi-Al) on antimonide heterostructures, where the epi-Al thin film is grown at either room temperature or below zero °C. A sharp superconducting transition at T ~ 1.3 K is observed in these epi-Al films, and the critical magnetic field follows the BCS (Bardeen-Cooper-Schrieffer) model. We further show that supercurrent states are achieved in Josephson junctions fabricated in the epi-Al/antimonide heterostructures with mobility $\mu \sim 1.0 \times 10^6$ cm^2/vs, making these heterostructures a promising platform for the exploration of Josephson junction effects for quantum microelectronics applications, and the realization of robust topological superconducting states that potentially allow the realization of intrinsically fault-tolerant qubits and quantum gates.

Aluminum (Al) as a superconductor is widely used in Josephson junctions (JJ) [1,2] and superconducting high Q resonators [3]. In recent years, much work has been devoted to epitaxially-grown Al (epi-Al) on semiconductors for achieving an interface of the highest quality between Al and the semiconductor, which should help realize topological superconductivity [4,5] and Majorana zero modes [6-8]. Examples include epi-Al on InAs or InSb nanowires for hard superconducting gaps [9,10], epi-Al on InAs quantum wells (QWs) [11-14] for planar JJs [15], and epi-Al on Si for quantum computing applications [16].

So far, less work has been carried out on epi-Al on antimonide heterostructures, in particular the InAs/GaSb type-II heterostructures. InAs/GaSb is a unique material system [17]. Depending on the thickness of InAs and GaSb quantum wells, the material can be a conventional semiconductor, a zero-band gap semimetal, or an inverted-band gap quantum spin Hall insulator [18,19]. The latter is of particular interest, since Majorana zero modes can be achieved at zero magnetic field in JJs mediated by the edge channels in a quantum spin Hall insulator [20]. This will simplify the design of topological qubits [21] and offer great promise of eventually achieving fault-resistant universal quantum computing.

Herein we first present results of our recent work of epitaxially-grown Al on InAs/GaSb type-II heterostructures, where the epi-Al thin film is grown at room temperature. A sharp superconducting transition at T ~ 1.3K is observed in the epi-Al film, and the critical magnetic field follows the BCS (Bardeen-Cooper-Schrieffer) model. We then present results for a JJ fabricated in a different epi-Al/antimonide heterostructure, where the starting growth temperature of the epi-Al layer is below 0 $^{\circ}$C. For this structure an InAs QW with mobility $\mu \sim$

1.0×10^6 cm^2/vs is realized. Supercurrents states are observed in this JJ. Moreover, near the critical current, a multi-switching behavior is observed. A two effective junctions model is proposed to explain this behavior. The observed large mobility, combined with the strong spin-orbit coupling of InAs, and the evidence of a superconducting proximity effect, make the structure an ideal candidate for the realization of non-Abelian states useful for quantum computations, given that disorder (low mobility) has emerged as the main obstacle toward the robust establishment and clear detection of such states.

In this work, an unintentionally doped GaSb wafer is used as the substrate for all the materials growth. The growth sequence of InAs/GaSb heterostructures is as follows. After a GaSb buffer layer (600 nm thick) and a short-period superlattice of GaSb/AlSb QWs, a 200-nm-thick Al$_{0.33}$Ga$_{0.67}$Sb potential barrier layer is grown. For the first structure the growth is then followed by InAs (13 nm) and GaSb (5 nm) double quantum wells and an AlSb (10 nm) potential barrier layer. At this point, effusion cells are brought to idle temperature and the substrate heater is turned off. After cooling the wafer completely overnight, the Al cell is reheated. Then, the final 30-nm-thick Al layer is grown on top of the AlSb layer.

The as-grown material is structurally characterized using aberration-corrected scanning transmission electron microscopy (AC-STEM) using an FEI Titan™ G2 80-200 STEM with a Cs probe corrector and ChemiSTEM™ technology, operated at 200keV. TEM samples are prepared using a Thermo Fisher Helios G-5 plasma FIB (PFIB) with Xe$^+$ ions at a temperature of -160 ℃. The cryogenic PFIB condition is to avoid the FIB induced AlGa epi-growth artifact, which could

happen unintentionally [22]. High-angle annular dark-field (HAADF) STEM imaging is used for structural analysis. More details can be found in Ref. [22].

Fig. 1a shows a cross section STEM image. It is evident that the Al layer is continuous but not uniform. Instead, large Al islands are formed. This is consistent with atomic force microscopy (AFM) results (Fig. 1b). Here, AFM scans are carried out in an area of 5×5 μm^2 to examine the surface morphology. Watershed masking through the software Gwyiddion is performed to isolate and separate the Al islands. The average equivalent disc radius is 54.7 nm. The surface roughness values are calculated by standard surface roughness equations and performed on a larger scan representative of the full dataset, and an RMS roughness of 5.86 nm is deduced.

Figure 1(c) shows a HAADF STEM image of the heterostructures in Figure 1a. Perfect epitaxial interfaces are seen between InAs, GaSb, and AlSb, respectively. More importantly, Al forms epitaxially with the AlSb layer underneath (the top-right inset), with orientations Al(110)//AlSb(001) and Al[1,−1,0]//AlSb[1,−1,0]. This epitaxial relationship is determined by analyzing the high-resolution STEM image and accompanying fast-Fourier transform (FFT) pattern in the top-left inset.

A specimen of size $\sim 5 \times 5$ mm^2 is then cleaved from the as-grown wafer for electronic transport characterization. Indium is placed along the edges and corners for ohmic contacts. Low frequency (~ 11 Hz) phase lock-in amplifier technique is used for the sample resistance measurements. For the DC current-voltage (I-V) characterization, a Keithley 238 source meter is used. All low temperature measurements are carried out in a pumped ^{3}He system.

Fig. 1d shows the four-terminal resistance R_{xx} as a function of temperature. At high temperatures, the resistance is nearly constant, ~ 1 Ω. At T ~ 1.3 K, R_{xx} drops sharply and reaches the zero-resistance value, when the Al thin film becomes superconducting. The range of temperature over which R_{xx} drops is only 20 mK, indicating a high quality of the epi-Al film and uniform transition temperature across the whole specimen.

To further characterize the superconducting properties in our sample, we measure R_{xx} as a function of magnetic field perpendicular to the epi-Al plane, from which the critical magnetic field B_c is deduced. In Fig. 1e, we plot B_c as a function of temperature. It follows the BCS formula $B_c = B_{c0} \times (1-(T/T_c)^2)$ [23], from which a zero-temperature critical magnetic field $B_{c0} = 43.4$ mT and a critical temperature of 1.23 K (which is consistent with that in Fig. 1d) are obtained.

To summarize the results above, we have achieved high quality Al epi-growth on InAs/GaSb type-II heterostructures. In the following, we will present results for a JJ made of epi-Al on a different heterostructure.

The growth structure of this second heterostructure is shown in Fig. 2a. It is based on the one used in Ref. [24] to achieve the highest electron mobility of two-dimensional gas (2DEG) in an InAs QW. In growing this structure, after the GaSb buffer layer, superlattices layer, and $Al_{0.33}Ga_{0.67}Sb$ bottom potential barrier, an InAs QW of 21 nm thick is grown, followed by an AlSb (20nm) potential barrier and a 5 nm thick GaSb 5 cap layer. The 2DEG is localized in the

InAs QW. Two identical structures are gown, one with a 30-nm epi-Al layer (Fig. 3a) and the other without (Fig. 2a). In growing the epi-Al layer, the substrate is rotated towards the cryo-pump so that the substrate temperature is lowered below 0 °C before the Al layer growth [24].

We first examine low temperature electronic characterizations of the 2DEG in the InAs QW without epi-Al. In Fig. 2b, we show the magnetoresistance R_{xx} and Hall resistance R_{xy} as a function of magnetic field; data are taken at the temperature of 0.3 K. Well-developed Shubnikov-de Haas oscillations and integer quantum Hall effect are observed in the low and high B regimes, respectively, demonstrating the high quality of the heterostructure. An electron density of $n = 5.4 \times 10^{11}$ cm^{-2} and mobility $\mu \sim 1.0 \times 10^6$ cm^2/vs are obtained from the R_{xx} and R_{xy} data. These values are comparable to those reported in InAs two-dimensional gas (2DEG) also grown on GaSb substrates [25-28], corroborating the high quality of our antimonide heterostructures. Using an effective mass of 0.03 m_e [25], we deduce an electron mean free path $L_{mfp} = 12$ μm and Fermi velocity of $v_F = 7.1 \times 10^5$ m/s.

We now examine the superconducting transition of the epi-Al thin film grown below 0 °C. Again, a specimen of size $\sim 5 \times 5$ mm^2 is cleaved from the wafer for electronic transport characterization. Fig. 3b shows the temperature dependence of four-terminal sample resistance. A superconducting transition is observed around 1.3 K. Different from the epi-Al film grown at room temperature, the resistance is extremely low, about 0.12 Ω. This lower resistance is likely due to an improved uniformity of the Al film grown at lower temperatures. R_{xx} as a function of B field is shown in Fig. 3c, from which a critical magnetic field $B_c \sim 5$ mT is obtained.

JJs are fabricated in this epi-Al-antimonide heterostructure. We use photoresist developer MF319 to etch off the Al in the junction region. An SEM image of a JJ is shown in Fig. 4a. The length of the junction (i.e., the separation between the two Al electrodes) L is about 2 μm, and the width 12.5 μm. Using the v_F value obtained above and an Al superconducting gap of $\Delta_{Al} = 1.76 K_B T_c \approx$ 0.23 meV ($T_c \approx 1.3K$), a superconducting coherence length $\xi_0 \equiv \hbar v_F / \Delta_{Al} \approx 2.0$ μm is deduced. So, in our JJ, $\xi_0 \sim L << L_{mfp}$, i.e., roughly in the short ballistic regime.

Furthermore, it is clearly seen that the color and the morphology of the junction region are different from that of the two large Al electrodes (Fig. 4b). The darker color in the region is most likely due to the static electromagnetic effect from the electron beam. EDS analysis (Fig. 4c) corroborates that aluminum is etched off in the junction region. Indeed, the shape of the junction is evident in the Al EDS image, while for In, Ga, and Sb a uniform distribution is displayed. We attribute the Al noise in the background to the underlying Al present in AlSb and AlGaSb layers. Additionally, we measure the depth of the etch to be ~ 40 nm, indicating that both the epi-Al and top GaSb layers are removed. This leaves the 2DEG in the InAs QW as the only conduction channel between the two Al electrodes. Finally, a much larger junction resistance in the normal state (~ 12 Ω, Fig. 4d) compared to that of the epi-Al layer (Fig. 3b) also corroborates the conclusion that aluminum is etched off in the junction region.

The temperature dependence of the junction resistance R_{xx} displays two superconducting transitions (Fig. 4d). The first occurs at $T_c \sim 1.5$ K when the epi-Al thin film become superconducting. It is slightly higher than the bulk Al thin film superconducting transition temperature of 1.3 K (Fig. 3b). This larger T_c is probably due to the epi-Al electrodes becoming

more amorphous [29] through device fabrication, as demonstrated in Fig. 4b. The second transition occurs at ~ 1.2 K, presumably when the 2DEG channel in the junction itself becomes superconducting.

The ability to induce superconducting correlations into an InAs QW with such high mobility is an important advance toward the realization of topological superconducting states supporting non-Abelian states given that disorder has emerged as the main obstacle toward the attainment of such states [30]. Given the potential of non-Abelian states for the realization of fault tolerant qubits and gates, the availability of superconductor-semiconductor heterostructure based on InAs QWs with such a large mobility would be an important contribution toward quantum computing.

The current-voltage (I-V) curve of the JJ is measured at zero magnetic field and shown in Fig. 4e. The current is swept in the up direction. Overall, the I-V curve behaves as expected in a typical JJ. In the large current regime (I > 120 μA), the I-V curve is linear, and the sample is in the normal state. Below a critical current of I_c ~ 105 μA, the dc voltage across the two Al electrodes V_{dc} is zero, and the JJ is in the supercurrent states.

Examining the data carefully, it is clearly seen that, near the critical current when the voltage jumps to a non-zero value, a multi-switching behavior is observed (Fig. 4e). This multi-switching behavior can be understood by invoking a model of two effective Josephson junctions (Junctions A and B, in Fig. 4e) with different critical currents and normal-state resistances. For Junction A, the critical current is I_c^A ~ 105 μA and the normal state resistance is R_N^A ~ 0.8 Ω (obtained from a linear fit of the data points marked by the red open squares). For Junction B, the

values are $I_c^B \sim 5$ μA and $R_N^B \sim 8$ Ω, respectively. As the current is swept from 0, at beginning it flows almost exclusively through Junction A, due to a much larger critical current this junction can accommodate. When the current reaches a value larger than I_c^A, Junction A becomes non-superconducting and a sizable portion of the current starts to flow through Junction B, which is still superconducting. This redirection of current may bring the current through Junction A below its critical value, and Junction A becomes superconducting again/ Consequently, a certain amount of the current now flows back to Junction A, until Junction A becomes normal again. This dynamic process of current from Junction A to B and then back A is consistent with the switching between the low resistance state and the high resistance state observed between ~ 105 and ~ 115 μA, see Fig. 4(e). Such switching behavior stops after the current is large enough and both Junctions A and B become normal. Beyond this point, the I-V curve becomes linear and there is no multi-switching behavior, as observed in Fig. 4e. We further notice here that the normal state resistance when both Junctions A and B are non-superconducting is smaller than that (~ 12 Ω) in Fig. 4d, suggesting that in the current regime we have measured the Al electrodes are still superconducting.

The time-averaged voltage-current (V-I) characteristic for the scenario above can be quantitatively described using an effective RSJ (resistively shunted junction) model, as depicted in Fig. 5a, where the cross (X) represents an ideal Josephson junction and the solid rectangular the junction's resistance. For an individual junction, the V-I characteristic can be written as $V = R_N \times I \times \Theta(I - I_c)$. Here $\Theta(x)$ is a step function, $\Theta(x) = 0$ for $x \leq 0$ and $\Theta(x) = 1$ for $x > 0$. The V-I trace for Junction A (B) without Junction B (A) is shown as the dashed line in Fig. 5b. With two junctions co-existing (Fig. 5a), the total voltage $V = R_N^A \times I \times \Theta(I - I_c^A) + R_N^B \times I \times \Theta (I -$

$I_c^A - I_c^B$), as marked by the solid line. The placing of the second junction in series with the resistive channel of the first junction, allows the RSJ model to capture, on average, the effect of the current's dynamical switching between the two superconducting channels when $I_c^A < I < I_c^A + I_c^B$, as described above. The overall shape of the V-I obtained with the proposed RSJ model agrees well with the experimental observations.

Below, we argue how the two effective junctions can form in our device structure. As shown in Fig. 4a, the separation between the two Al electrodes at the edges (~ 2 μm) is quite shorter than that in the central region (~ 6.5 μm). Consequently, we can expect that the region close to the edges will form one junction (Junction A) with a large critical current (105 μA) and a small normal-state resistance (0.8 Ω), while the central part will form a junction (Junction B) with a small critical current (5 μA) and a large normal-state resistance (8 Ω). With these assignments, we calculate the values of eI_cR_N for the two junctions, and find them to be~ 84 and 40 μeV, respectively. These values are smaller than the Al superconducting gap of $\Delta_{Al} \sim 230$ μeV, indicating a low interface transparence between the epi-Al layer and InAs quantum well. This is not unexpected considering there exists an AlSb up potential barrier of 20 nm thick between the two materials. A thinner AlSb should help enhance the interface transparency.

In summary, we have achieved high quality epi-growth of aluminum on antimonide heterostructures. A sharp superconducting transition is observed in our epi-Al thin film. The critical magnetic field displays a temperature dependence that follows the conventional BCS theory. We further show that the epi-Al antimonide heterostructures is a promising material

platform for exploring Josephson effects for superconducting microelectronics and quantum information applications.

References:

[1] R. Harris et al., Phys. Rev. B 80, 052506 (2009).
[2] F. Arute et al., Nature 574, 505 (2019).
[3] C.J.K. Richardson et al., Supercond. Sci. Technol. 29, 064003 (2016).
[4] M. Sato and Y. Ando, Rep. Prog. Phys. 80, 076501 (2017).
[5] B. A. Bernevig and T. L. Hughes, Topological Insulators and Topological Superconductors (Princeton University Press, Princeton, NJ, 2013).
[6] R.M. Lutchyn, J.D. Sau, and S. Das Sarma, Phys. Rev. Lett. 105, 077001 (2010).
[7] Y. Oreg, G. Refael, and F. von Oppen, Phys. Rev. Lett. 105, 177002 (2010).
[8] M. Aghaee et al., Phys. Rev. B 107, 245323 (2023).
[9] W. Chang et al., Nature Nanotechnology 10, 232–236 (2015)
[10] Önder Gül et al., Nano Lett. 17, 2690 (2017).
[11] J. Shabani et al., Phys. Rev. B 93, 155402 (2016).
[12] E. Cheah et al., Phys. Rev. Materials 7, 073403 (2023).
[13] A. Banerjee et al., Phys. Rev. B 107, 245304 (2023).
[14] P. Yu et al., preprint arXiv:2404.09901 (2024).
[15] F. Pientka et al., Phys. Rev. X 7, 021032 (2017).
[16] B. M. McSkimming et al., J. Vac. Sci. Technol. A 35, 021401 (2017).
[17] C.X. Liu et al., Phys. Rev. Lett. 100, 236601 (2008).
[18] Y. Jiang et al., Phys. Rev. B 95, 045116 (2017).
[19] W. Yu et al., New Journal of Physics 20, 053062 (2018).
[20] H. Wang et al., Nature Materials 15, 38 (2016).
[21] D. Aasen et al., Phys. Rev. X 6, 031016 (2016).
[22] D.P. Cummings et al., Microscopy and microanalysis 29, 138-144 (2023)
[23] M. Tinkham, Introduction to Superconductivity (McGraw-Hill, New York, 1996).
[24] C.-C. Yeh et al., Phys. Rev. Materials 7, 224801 (2023).
[25] T. Tschirky et al, Phys. Rev. B 95, 115304 (2017).
[26] B. Shojaei et al., Phys. Rev. B 94, 245306 (2016).
[27] C. Thomas et al., Phys. Rev. Materials 2, 104602 (2018).
[28] S. Komatsu et al., Phys. Rev. B 105, 075305 (2022).
[29] K. Knorr and N. Barth, Solid State Commun. 6, 791 (1968).
[30] S. Ahn et al., Phys. Rev. Materials 5, 124602 (2021).
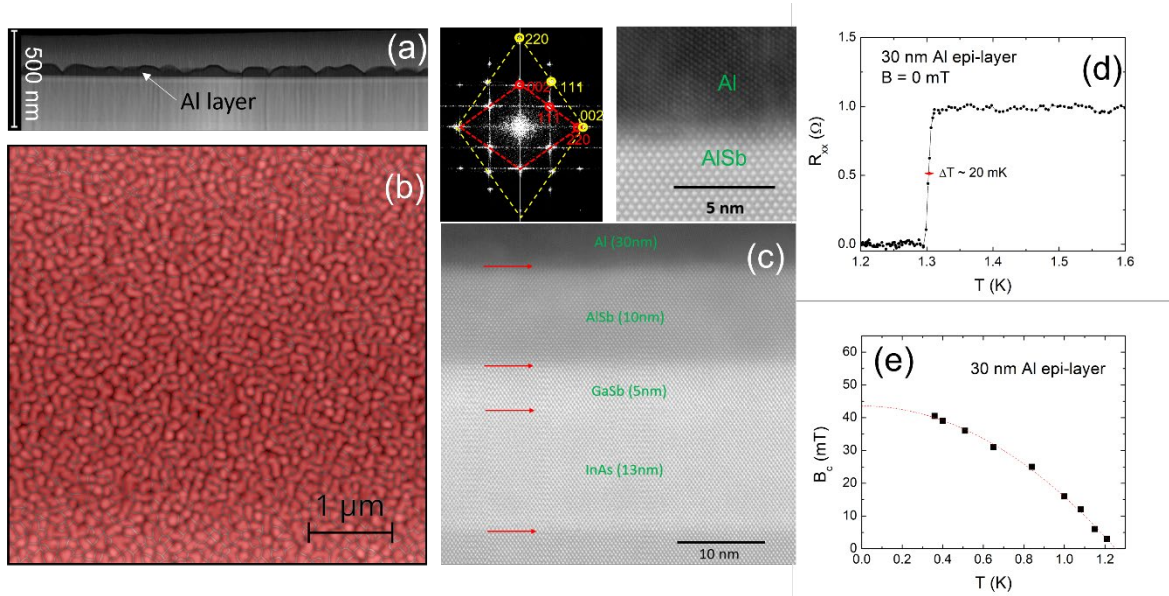
Figures and figure captions

Figure 1

Fig. 1 Structural and electronic characterizations of epi-Al thin film on an AlSb/GaSb/InAs heterostructure. (a) Cross-section image of the epi-Al layer, the scale bar is 500nm. (b) AFM image of epi-Al film over a 5×5 μm^2 area. (c) HAADF STEM images of the heterostructures in Figure 1a. The top right inset shows the high-resolution STEM image of Al and AlSb epitaxial relationship. The accompanying fast-Fourier transform pattern is shown in the top-left inset. (d) Sample resistance R_{xx} as a function of temperature (T) at B = 0 T in the epi-Al layer. A superconducting transition is seen at T ~ 1.3K. (e) Critical magnetic field (B_c) as a function of temperature in the epi-Al layer. The red line is a fit to the BCS formula.
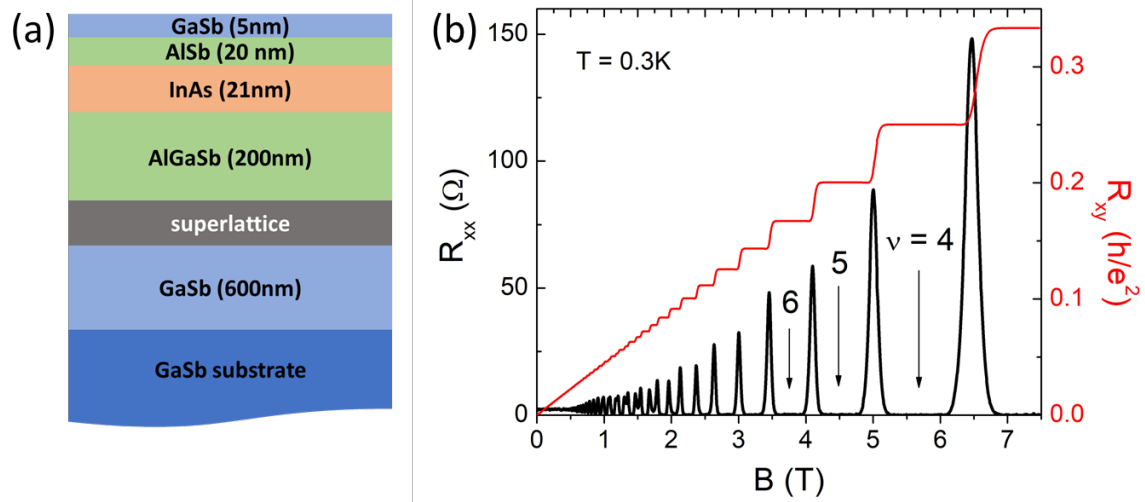
Figure 2

Fig. 2 (a) Growth structure of a high-mobility InAs quantum well structure. (b) Magnetoresistance R_{xx} and Hall resistance R_{xy} measured in this quantum well. Quantum Hall states at Landau level filling ν = 4, 5, 6 are marked.
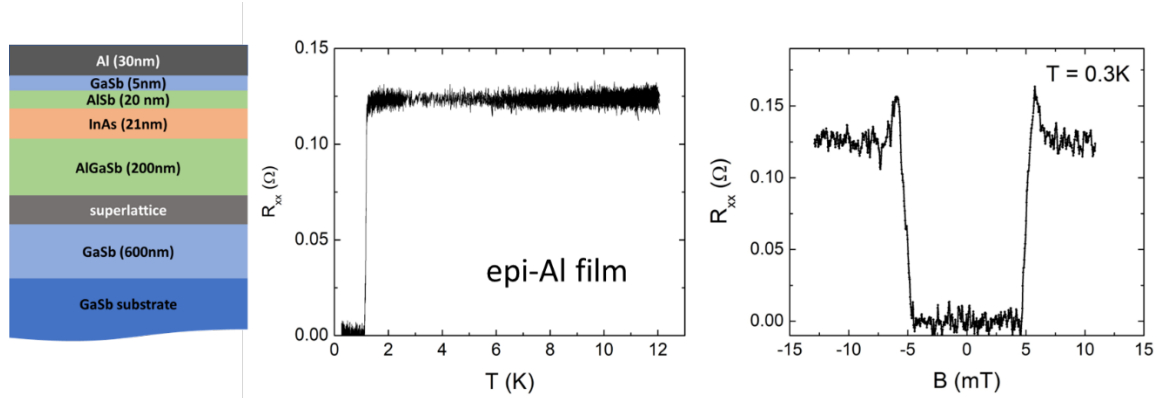
Figure 3

Fig. 3 (a) Growth structure of epi-Al on the InAs QW antimonide heterostructure. (b) Sample resistance R_{xx} as a function of temperature at B = 0 T in the epi-Al layer. A superconducting transition is seen at T ~ 1.3 K. (c) Magnetoresistance of the epi-Al layer measured at T = 0.3 K. R_{xx} = 0 Ω around B = 0 T. It jumps to a finite value at ~ ±5 mT.
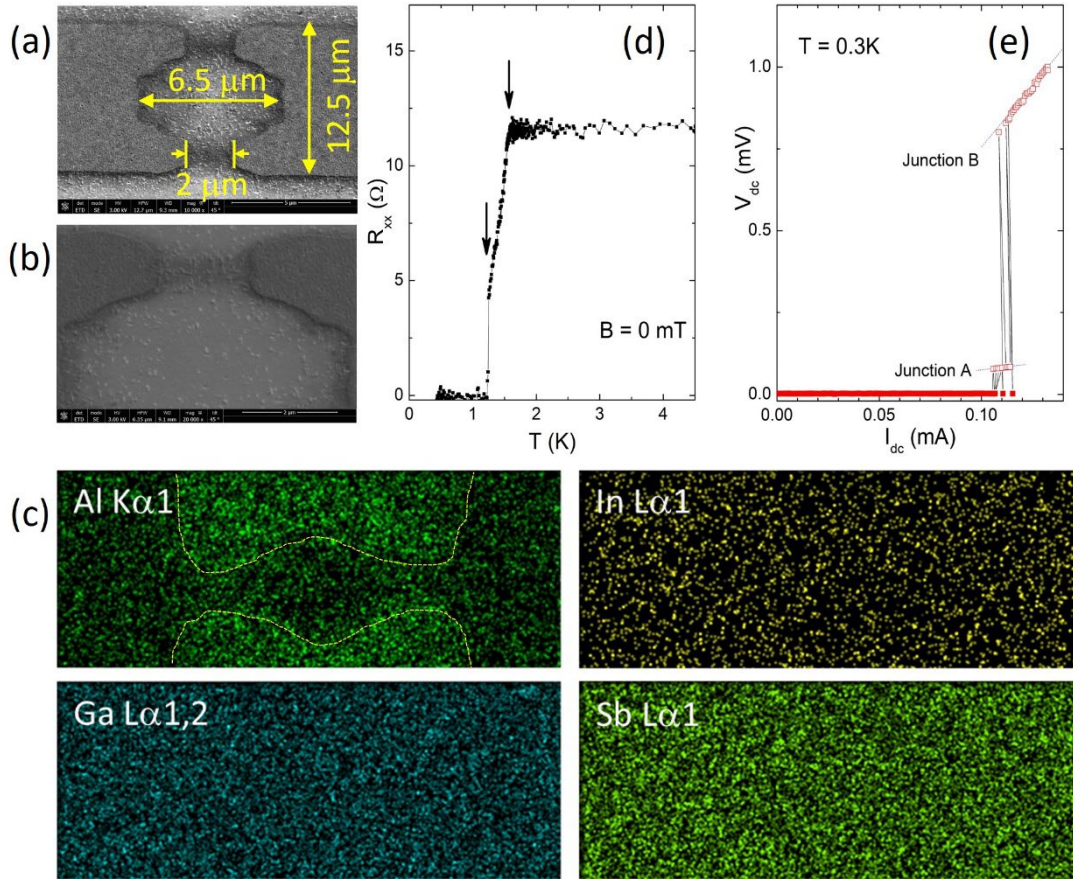
Figure 4

Fig. 4 (a) SEM image of a large Josephson junction (JJ). (b) Zoomed image of Fig. 4(a). (c) EDS maps of Al Kα, Ga Lα, In Lα, and Sb Lα, extracted from spectral image with selected EDS energy windows for each element. The dotted green line is a guide to the eye. (d) Superconducting transition in the JJ, marked by the arrows. (e) I-V curves for current sweeping up from zero voltage. The dashed lines are liner fits, from which the normal resistance is obtained for Junction A and B.
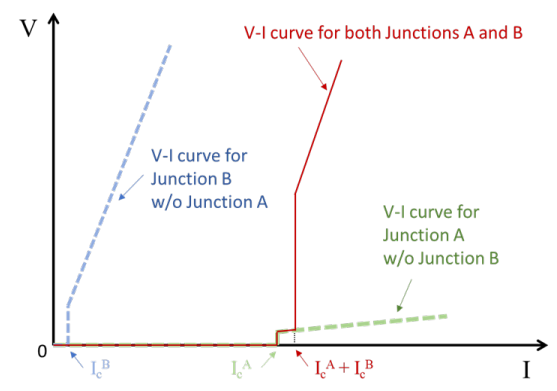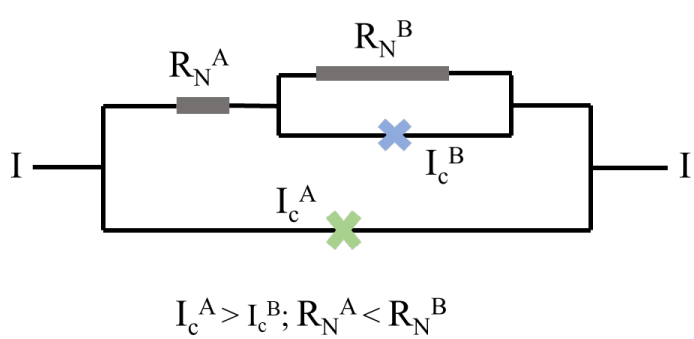
Fig. 5 (a) Effective RSJ model for our device with two Josephson junctions. The cross (X) represents a Josephson junction and the solid rectangular the junction resistance. (b) Schematic of V-I curves. The green/blue dashed line represents the V-I curve for individual Junction A/B, respectively. The total V-I curve for the two co-existing junctions in Fig. 5(a) is depicted by the red solid line.